© Indian Academy of Sciences

# Substantial enhancement in thermoelectric figure-of-merit of half-Heusler ZrNiPb alloys

AMARDEEP SAGAR[1,†], AMAN BHARDWAJ[1,4,†], MANOJ LAMBA[1,†], ANDREI NOVITSKII[2], VLADIMIR KHOVAYLO[2,3] and SATYABRATA PATNAIK[1,*]

[1] School of Physical Sciences, Jawaharlal Nehru University, New Delhi 110067, India
[2] National University of Science and Technology 'MISiS', Moscow 119049, Russia
[3] Belgorod State University, Belgorod 308015, Russia
[4] *Present Address:* Chemistry Section, Department of Education in Science and Mathematics (DESM), Regional Institute of Education (RIE), Bhubaneswar, India
*Author for correspondence (spatnaik@mail.jnu.ac.in)

[†]These authors have contributed equally to this study.

**Abstract.** Ternary half-Heusler (HH) alloys are under intense investigations recently towards achieving high thermoelectric (TE) figure-of-merit (ZT). Of particular interest is the ZrNiPb-based HH alloy, where an optimal value of ZT $\sim$ 0.7 at 773 K has been achieved by co-doping Sn and Bi at Pb site. In this work, we identify an excellent ZT of 1.3 in $ZrNi_{1+x}Pb_{0.38}Sn_{0.6}Bi_{0.02}$ ($x = 0.03$, at 773 K) composite alloy. This is achieved by synergistic modulation of electronic as well as thermal properties via introduction of minor phase of full-Heusler (FH) in the HH matrix through compositional tuning approach. These Ni-rich $ZrNi_{1+x}Pb_{0.38}Sn_{0.6}Bi_{0.02}$ ($0 \leq x \leq 0.07$) alloys were synthesized via energy efficient and time-curbed techniques that involved Arc melting followed by consolidation via spark plasma sintering. These alloys were characterized by XRD and SEM, which show formation of nanocomposites comprising of HH matrix phase and FH secondary minor phases. Enhancement in ZT is mainly attributed to a synchronized increase in power factor ($\sim$42%) and $\sim$25% decrease in its thermal conductivity. Here, TE compatibility factor ($S$) was also calculated for all samples. The value of $|S| \sim 2.7 \, V^{-1}$ (at 773 K) is observed for $x = 0.03$, which is $\sim$17% higher than bare HH composition ($x = 0.0$). The theoretically calculated TE device efficiency of best-performing sample $ZrNi_{1.03}Pb_{0.38}Sn_{0.6}Bi_{0.02}$ is estimated to be $\eta \sim 13.6\%$. Our results imply that deliberately controlled fine tuning in compositions of HH compounds through compositional tuning approach would lead to novel off-stoichiometric HH phases with enhanced ZT value for efficient TE device fabrication.

**Keywords.** Thermoelectric materials; compositional tuning approach; half-Heusler; spark plasma sintering; nanocomposite; thermoelectric figure-of-merit.

## 1. Introduction

Thermoelectric (TE) materials and devices hold great promise as alternative sources of energy for garnering electricity from waste heat [1]. However, large-scale commercialization of TE materials has remained limited due to poor conversion efficiency and high cost. The conversion efficiency is assessed from the TE figure-of-merit $ZT = \alpha^2 \sigma T/\kappa$, where $\kappa$ is total thermal conductivity, $\sigma$ is electrical conductivity, $T$ is the temperature (Kelvin) and $\alpha$ is Seebeck coefficient. Due to the interdependence of all three parameters, enhancement in ZT has been a challenging task over the years [2]. Along with the ZT optimization, estimation of TE compatibility factor ($S$) is an important factor that is useful for compatible segmentation in TE devices to attain maximum

TE device conversion efficiency ($\eta$) for waste heat recovery applications. The conversion efficiency of TE devices mainly depends on the ZT value at operating temperature and the theoretical conversion efficiency of TE device ($\eta$) is related to hot temperature ($T_h$), cold temperature ($T_c$) and $ZT_{avg}$, which is the average value of ZT [3,4]. Further, the compatibility factor ($S$) is the most important parameter for estimation towards finding the best-suited counterpart and to achieve maximum TE efficiency in TE device. With the advent of a new theoretical paradigm and significant advancement in processing technologies, several new pathways have been attained to decouple the TE parameters and thereby attain a high figure-of-merit and compatibility factor [3,4].

Half-Heusler alloys (HH) are among the emerging TE materials for varied applications, particularly in the mid-

temperature (400–800°C) range. The main advantages of HH alloys include high mechanical strength, moderately good power factor (PF = $\alpha^2\sigma$) and high thermal stability for TE device fabrication. However, high thermal conductivity results in low ZT value in these materials [5]. In particular, *n*-type HHs such as ternary intermetallic (Ti/Zr/Hf)NiSn are considered potential candidates for waste heat recovery applications [6]. However their reported ZT value is still low ($\sim 0.3$ at 773 K) which prohibits commercial applications. Besides, the use of costly Hafnium makes them expensive for industrial applications [7]. Further possibility in enhancement of ZT for the (Ti/Zr/Hf)NiSn-based materials seems daunting as several approaches have been tried yet their thermal conductivity continues to be high due to the effect of bipolar conduction at higher temperatures [8]. Thus, the search for a new *n*-type HH material with high conversion efficiency has attracted considerable attention in the recent past.

In general terms, the thermal conductivity $\kappa$ has two main components which includes lattice ($\kappa_L$) as well as electronic ($\kappa_e$) contributions. The approach related to nanostructuring/nanocomposite has recently been established to be of substantial success in improving ZT due to a large reduction in lattice $\kappa_L$. The microscopic origin of such phenomena involving phonon scattering is reasonably well understood [9,10]. However, the overall increase in ZT attained thus far remains impractical for technological applications. Clearly, there is a need to couple this approach with clever enhancement in $\alpha$ without altering $\sigma$. Hence a new strategy has been envisaged, in which nanocomposites derived by compositional tuning need to be optimized for a reasonable decrease in $\kappa_L$ along with a simultaneous increase in Seebeck coefficient [11,12]. Generally, the $\kappa_L$ value is dependent on the crystal lattice and microstructure. Therefore, a compositional tuning in HH materials can play a vital role in reducing the $\kappa_L$. Several recent papers have reported that formation of a full Heusler ((Ti/Zr/Hf)Ni$_2$Sn) inclusion phase in HH ((Ti/Zr/Hf)NiSn) matrix can lead to the desired result [11–15]. Both FH and HH have FCC structure, which helps to create *in-situ* formation of nanocomposites leading to lowering of $\kappa_L$. Furthermore, it is reported that the HH/FH band alignment leads to optimized carrier mobility for higher electrical conductivity. Most importantly such compositional tuning approaches have also been reported to increase Seebeck coefficient via intra-matrix electronic structure modifications. Thus it is established that all three parameters of ZT dependence can be optimized simultaneously by following compositional tuning of HH alloys [16,17].

Of great current interest is the HH alloy based on the ZrNiPb system, where an optimized high ZT $\sim 0.75$ (at 873 K) has been reported via co-doping of Sn and Bi [18–20]. This enhancement in ZT is primarily assigned to the alloying effect of Sn on Pb, which results in a significant reduction in $\kappa_L$ while Bi doping tunes the carrier concentration for maintaining a high PF. The question is whether it can be further increased by following compositional
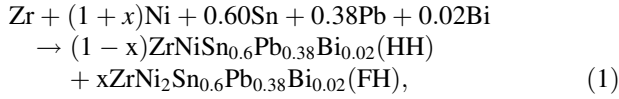
variation techniques as implemented in MNi$_{1+x}$Sn (M = Ti/Zr/Hf) systems [11–15]. In such nanocomposite systems, the inclusion of precipitated FH phase into HH matrix is caused due to phase segregation processes. In such nanocomposites reduction in $\kappa_L$ value can be attributed to various kinds of scattering mechanism, which includes grain boundary scattering, point scattering and alloy scattering [11–15]. Furthermore, the improved electronic properties observed in these nanocomposites due to compositional tuning leads to band-structure engineering, which has been successfully demonstrated as an efficient approach for achieving high ZT of many TE materials [21]. With this evidence in mind, we intuitively understand that synthesis of an off-stoichiometric ZrNiPb-based HH/FH nanocomposite material could possibly lead to a higher ZT value.

Here, in this work, we carry out detailed synthesis and characterization of FH and HH nanocomposite to test the above hypothesis. We note that ZrNiPb and ZrNi$_2$Pb are the corresponding HH and full-Heusler components. Further, in order to obtain a nanocomposite of HH phase having FH inclusions with multiple length scales, Ni concentration was varied in ZrNi$_{1+x}$Pb$_{0.38}$Sn$_{0.6}$Bi$_{0.02}$ ($0 \leq x \leq 0.07$) compositions. We observe a large decrease in $\kappa_L$ ($\sim 25\%$ for ZrNi$_{1.03}$Pb$_{0.38}$Sn$_{0.6}$Bi$_{0.02}$), which has been achieved due to tuning of various scattering mechanisms caused by a large difference in atomic mass, embedded FH inclusion and HH/FH interface. Also a substantially improved PF ($\sim 42\%$ for composition; $x = 0.03$) has been obtained. This is due to structural similarities between HH and FH, which create HH/FH interface for optimizing the carrier mobility. An excellent value of ZT = 1.3 at 773 K has been attained for ZrNi$_{1.03}$Pb$_{0.38}$Sn$_{0.6}$Bi$_{0.02}$, which is the highest ZT value in ZrNiPb-based HH compositions.

## 2. Experiments

High purity of lead (Pb; 99.99%, Alfa Aesar, granules), nickel (Ni; 99.8%, Alfa Aesar, powder), tin (Sn; 98.0%, CDH shots), zirconium, (Zr; 98.0%, CDH, powder), and bismuth (Bi; 99.99%, Alfa Aesar shots) were weighed in their respective stoichiometric ratio followed by arc melting under argon atmosphere. Here, 2 at. wt% additional Pb was weighed in each composition because in the arc melting process Pb gets partially evaporated. The ingots were melted three times followed by annealing in a sealed quartz tube at 1073 K for 7 days to obtain the phase stability. These annealed ingots were then subjected to mortar–pestle grinding followed by ball milling to get fine powder with reduced grain size. The powders were consolidated into highly dense pellets by using the spark plasma sintering (SPS) technique at 800°C and 50 MPa under high vacuum with a 10-min holding time in a graphite die of 12.7 mm diameter. A high vacuum is provided in SPS to achieve a very clean sample by avoiding the adsorptive gases and impurities which thereby prevents the oxidation of the

sample. The dense pellets obtained from samples by SPS were further annealed at 750°C for 2 days. The densities of as-grown samples were observed to be 97% of the theoretical density. As discussed already, the excess Ni effectively leads to the synthesis of nanocomposites of FH and HH components. This can be represented by the following chemical equation (1):

$$\begin{aligned}
Zr &+ (1 + x)Ni + 0.60Sn + 0.38Pb + 0.02Bi \\
&\rightarrow (1 - x)ZrNiSn_{0.6}Pb_{0.38}Bi_{0.02}(HH) \\
&+ xZrNi_2Sn_{0.6}Pb_{0.38}Bi_{0.02}(FH),
\end{aligned} \quad (1)$$

Structural characterization of the samples was done by X-ray diffraction technique (Rigaku Mini flex II) for the phase identification of $ZrNi_{1+x}Pb_{0.38}Sn_{0.6}Bi_{0.02}$ ($0 \leq x \leq 0.07$) samples. The microstructural characterization of the $ZrNi_{1+x}Pb_{0.38}Sn_{0.6}Bi_{0.02}$ alloys was performed using scanning electron microscopy (SEM). The actual atomic composition of alloys was estimated through energy dispersive spectroscopy (EDAX). The thermal diffusivities ($D$) of all the synthesized samples were measured by using a Laser flash apparatus (Lineseis; LFA 1000). Specific heat ($C_p$) along with density ($d$) was measured for all synthesized samples using the differential scanning calorimetry (DSC) instrument and Archimedes principle, respectively. The thermal conductivity was calculated using the relation $\kappa = D \times C_p \times d$. The electronic transport properties were measured by the ULVAC ZEM-3 instrument. Room temperature, carrier concentration ($n$) was measure by Van der paw method. The mobility ($\mu$) and ($n$) values were determined using the Hall effect measurement system in conjunction with a superconducting magnet system.

## 3. Results and discussions

### 3.1 *Structural characterization*

Figure 1 displayed the XRD of $ZrNi_{1+x}Pb_{0.38}Sn_{0.6}Bi_{0.02}$ ($0 \leq x \leq 0.07$) composite samples. XRD of $ZrNiPb_{0.38}Sn_{0.6}Bi_{0.02}$ shows all the peaks of HH (space group F4-3m; no. 216; JCPDS card no. 00-023-1281) with a small trace of Pb as an impurity phase. The Pb impurities are expected as all the samples are vacuum sealed in a quartz tube before annealing, and hence Pb becomes vapour during the annealing treatment and remains unreacted to a small extent. Importantly, the XRD of $ZrNi_{1+x}Pb_{0.38}Sn_{0.6}Bi_{0.02}$ ($0 \leq x \leq 0.07$) composite samples clearly reveals the presence of FH (Fm3m; no. 225; JCPDS card no. 00-023-1282) phases along with HH and Pb impurity phase.

Post arc melting, liquid melt of $ZrNi_{1+x}Pb_{0.38}Sn_{0.6}Bi_{0.02}$ composite alloys, when cooled down, crystallizes to form a stable composite consisting of HH and FH components through phase separation [22–24]. Herein, the segregation of the FH and HH phases is produced due to excess concentration of Ni concentration [22–24].

The scanning electron microscopy (SEM) was performed in several samples but in figure 2, we focus on $ZrNi_{1.03}Pb_{0.38}Sn_{0.6}Bi_{0.02}$ which was identified with the best ZT for the entire series. The micrograph reveals a tightly packed microstructure of the HH phase along with *in-situ* FH precipitates. The EDX of the FH (white dotted circle) and HH (solid white square) regions confirm their composition. These results provide direct evidence of the formation of FH precipitates as a secondary phase in the HH matrix.

### 3.2 *Electronic transport properties*

Figure 3a and b plot the Seebeck coefficient and electrical conductivity as a function of temperature for all synthesized compositions. Here, all samples have negative value of α, which imply that these samples were *n*-type semiconductor. The α-value of $ZrNi_{1.03}Pb_{0.38}Sn_{0.6}Bi_{0.02}$ is $\sim -124.5\,\mu V\,K^{-1}$ at 323 K which is $\sim 24\%$ improved in contrast to $ZrNiPb_{0.38}Sn_{0.6}Bi_{0.02}$ HH ($\sim -100.7\,\mu V\,K^{-1}$ at 323 K). More importantly, an increase of $\sim 12\%$ was achieved in α at a higher temperature of 773 K which suits well for practical applications. We further note that for composite with $x = 0.07$, the value of α was noted to be lower (i.e., $\alpha \sim -139.7\,\mu V\,K^{-1}$ at 773 K) as compared to the $ZrNiPb_{0.38}Sn_{0.6}Bi_{0.02}$ (HH; $\alpha \sim -161.9\,\mu V\,K^{-1}$ at 773 K) that clearly reveals that composite had crossed over to greater metallicity as will be evident in the following discussion.

An enhanced value of α for $ZrNi_{1.01}Pb_{0.38}Sn_{0.6}Bi_{0.02}$ and $ZrNi_{1.03}Pb_{0.38}Sn_{0.6}Bi_{0.02}$ as compared to the HH alloy was obtained due to a reduced value of *n* at 323 K (i.e., $\alpha = \frac{8\pi^2 k_B^2}{3eh^2}m_e^* T(\frac{\pi}{3n})^{\frac{2}{3}}$). Table 1 displays the room temperature values of *n*, $\mu$ and Hall coefficient ($R_H$) for all samples. The room temperature mobility ($\mu$) is calculated via using the relation; $\sigma = ne\mu$. A decreasing value of *n* and increasing value of $\mu$ is observed in the samples having excess Ni concentration up to 0.03. This decrease in the *n*-value is counter-intuitive but has been evidenced in several other studies [11–15]. Indeed, a high value of *n* will be expected because of the addition of a semi-metallic FH phase in the semiconducting HH matrix [25]. In the literature, two theories have been proposed to explain the anomalous features achieved in these composite samples. Firstly, this decrease in *n*-value could be ascribed to the filtering of low-energy carriers through negligible barriers created at the phase boundaries of HH and FH [11–15]. This has been schematically explained by molecular orbital theory (MOT) in figure 4. A theoretical model by Faleev *et al* [25] also proposes that an energy barrier is generated at the interface of the metallic inclusion phase/semiconducting matrix phase due to band bending, which ultimately plays an important role as an energy filter for the carriers to have low energy, whereas the charge carriers having high energy remain unaffected. The same trends have also been discussed in the model proposed by Nolas *et al.* [26]. In terms
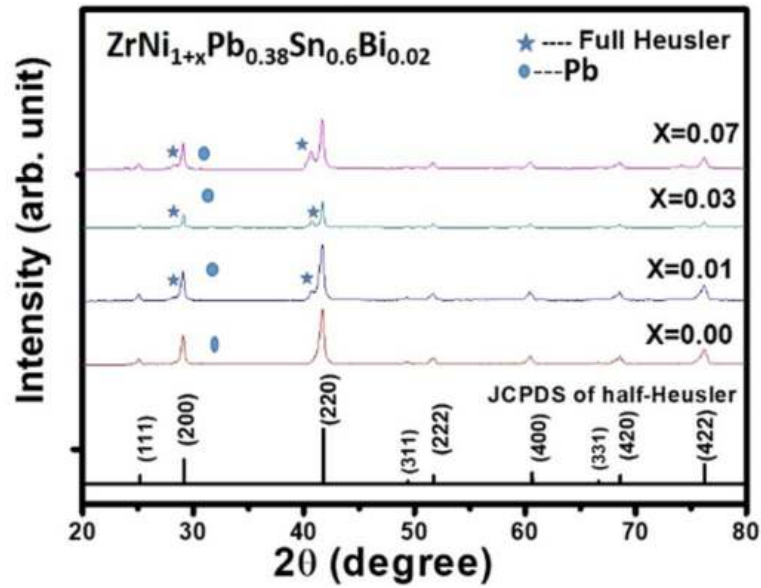
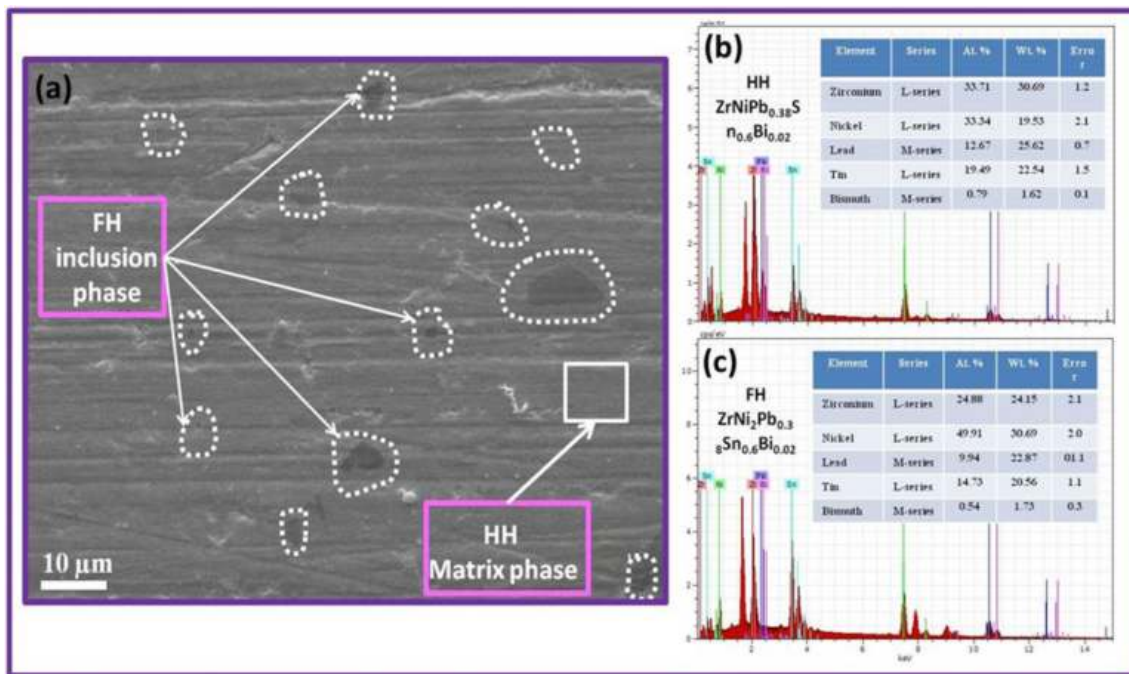**Figure 1.** XRD pattern of $ZrNi_{1+x}Pb_{0.38}Sn_{0.6}Bi_{0.02}$ ($0 \leq x \leq 0.07$) composites samples.



**Figure 2.** SEM image of best thermoelectric performing composite $ZrNi_{1.03}Pb_{0.38}Sn_{0.6}Bi_{0.02}$ at low-magnification display *in-situ* FH precipitate, indicated by white dotted circle and the matrix phase HH by solid white-square along with the EDX analysis.

of this theory, the enhancement of $\alpha$ in $ZrNi_{1.03}Pb_{0.38}Sn_{0.6}Bi_{0.02}$ as compared to $ZrNiPb_{0.38}Sn_{0.6}Bi_{0.02}$ HH can be linked to changes in scattering factor and reduced Fermi energy [27]. Herein, the Seebeck coefficient ($\alpha$) is given by

$$\alpha = \frac{\pi^2}{3} \frac{k_B}{e} \left(r + \frac{2}{3}\right)\left(\frac{1}{\xi}\right), \qquad (2)$$

where $\xi$ represents the reduced Fermi energy, Boltzmann constant ($k_B$) and $r$ implies the scattering factor. The decrease in $n$-value for $ZrNi_{1.03}Pb_{0.38}Sn_{0.6}Bi_{0.02}$ could therefore be hypothesized to be linked to a reduction in $\xi$ and an increase in $r$-value towards an overall increase in $\alpha$-value in contrast with HH alloys [28]. Although our data could be qualitatively explained through Nolas's model, a

**Table 1.** Hall measurement data for of $ZrNi_{1+x}Pb_{0.38}Sn_{0.6}Bi_{0.02}$ ($0 \leq x \leq 0.07$) composites samples.

| Nominal composition | $R_H$ $(10^{-2} \text{ m}^3 \text{ C}^{-1})$ | $n$ $(10^{20} \text{ cm}^{-3})$ | $\mu$ $(\text{cm}^2 \text{ V}^{-1} \text{ s}^{-1})$ |
|---|---|---|---|
| $x = 0.00$ | 1.50 | 4.16 | 29.4 |
| $x = 0.01$ | 1.86 | 3.36 | 30.52 |
| $x = 0.03$ | 1.91 | 3.26 | 41.43 |
| $x = 0.07$ | 1.48 | 4.21 | 44.69 |

relatively vigorous study will be required to explain it completely. Such decreasing value of $n$ leading to considerable enhancement in $\alpha$ has been reported in several earlier studies [11–15]. Here, it is necessary to discuss in more detail how the average crystallite size of investigated samples and crystallite size distribution may change with annealing temperature and how they affect their crystal structure and electronic properties. How was the effect of average crystallite size and crystallite size distribution on the electronic properties of the compounds under study taken into account? Mass transport, and especially oxygen transport, destroys the grains.

Figure 3b displays the temperature dependent $\sigma$ of $ZrNi_{1+x}Pb_{0.38}Sn_{0.6}Bi_{0.02}$ ($0 \leq x \leq 0.07$) composites. A decrease in $\sigma$ at 323 K was observed in $ZrNi_{1+x}Pb_{0.38}Sn_{0.6}Bi_{0.02}$ with $x = 0.01$ and 0.03 samples as compared to $ZrNiPb_{0.38}Sn_{0.6}Bi_{0.02}$ HH matrix. As displayed in table 1, an increasing value of carrier mobility ($\mu$) was observed with increasing Ni concentration in $ZrNi_{1+x}Pb_{0.38}Sn_{0.6}Bi_{0.02}$ composites. This increment in $\mu$ value may be due to the formation of FH which precipitated during the phase separation process. These FH nanoclusters offer a smooth pathway for charge carriers in electronic transport which is in agreement with published reports [11–15]. Focusing on high-temperature range, we find that at 773 K, the $\sigma$ of the $ZrNi_{1.03}Pb_{0.38}Sn_{0.6}Bi_{0.02}$ is $\sim 15\%$ higher than that of the $ZrNiPb_{0.38}Sn_{0.6}Bi_{0.02}$ HH matrix (figure 3b). This significant increase is observed due to the mobility contribution in conductivity which seems to have dominated over and above the carrier concentration contribution leading to an enhancement in $\mu$. In essence, increasing Ni concentration results in an enhancement in the value of $\mu$ for all composite samples (table 1). This can be interpreted as contributing to FH nano inclusions that provide facile pathway to the carriers for increasing the electronic transport. In figure 3b, we also note that $ZrNi_{1.07}Pb_{0.38}Sn_{0.6}Bi_{0.02}$ composite sample has $\sim 28\%$ enhanced value of electrical conductivity as compared to $ZrNiPb_{0.38}Sn_{0.6}Bi_{0.02}$ due to combined improvement in carrier concentration and mobility. Clearly significant increase in metallicity has happened for $x = 0.07$ that is reflecting low value of $\alpha$ as well.

Insightful understanding of transport properties can be achieved by using band-bending effects as elucidated by molecular orbital theory (MOT) diagram (figure 4). We know that the band structure of FH is quite similar to HH, as they have almost same composition with only difference of
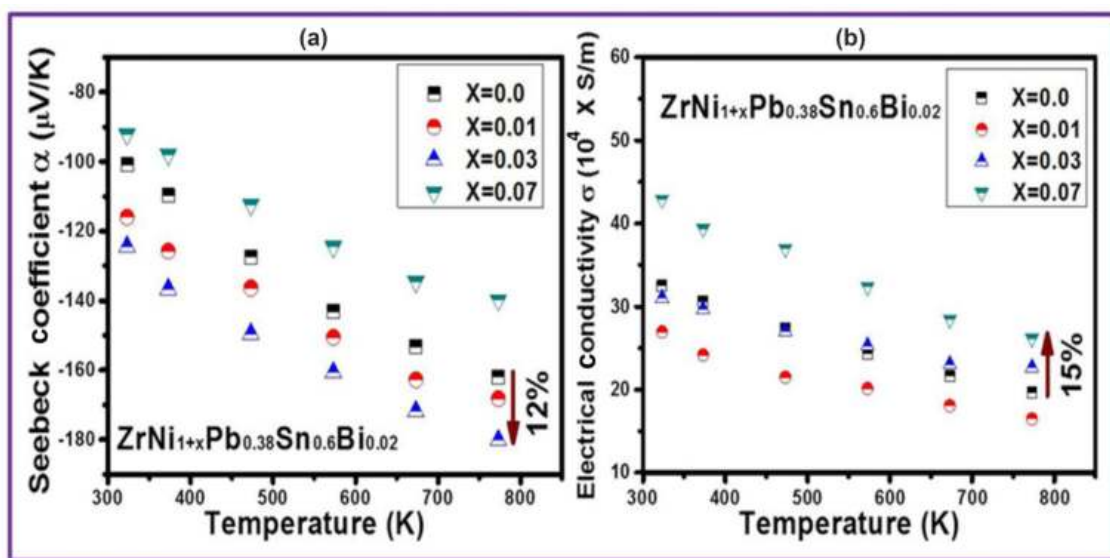


**Figure 3.** (a) Seebeck coefficient and (b) electrical conductivity of $ZrNi_{1+x}Pb_{0.38}Sn_{0.6}Bi_{0.02}$ ($0 \leq x \leq 0.07$) composites as a function of temperature.
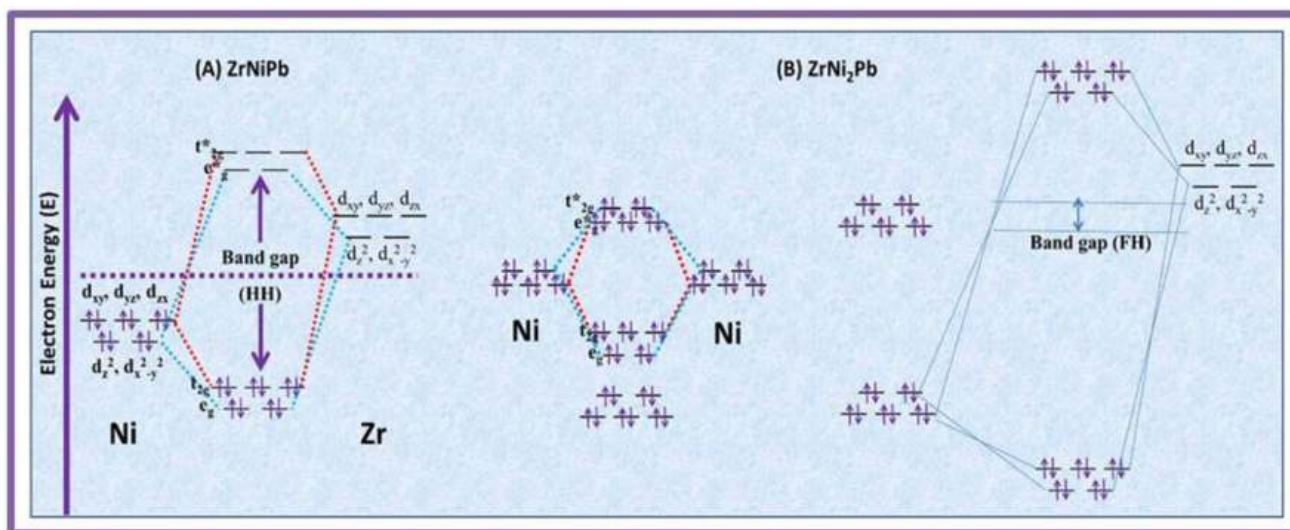
**Figure 4.** A representative molecular orbital theory (MOT) diagram for elucidating the development of FH (ZrNiPb) inclusion phase because of the incorporation of Ni atom in the empty tetrahedral site of HH phase (ZrNiPb).
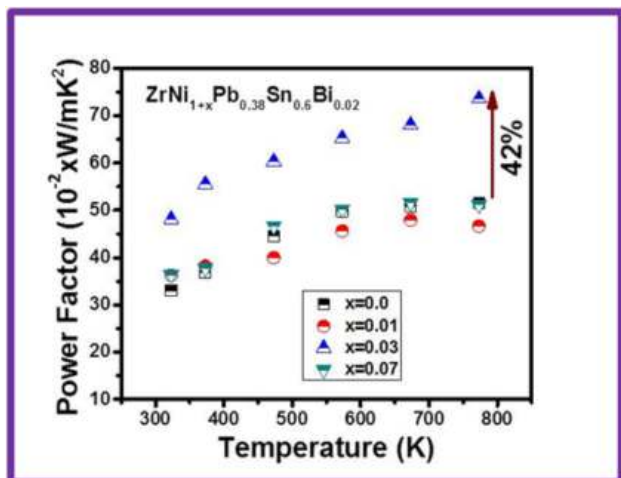


**Figure 5.** Temperature-dependent PF for all the composition of $ZrNi_{1+x}Pb_{0.38}Sn_{0.6}Bi_{0.02}$ $(0 \leq x \leq 0.07)$ composites samples.

a partially filled band due to one extra Ni atom in FH composition. But the bandgap of FH is less than HH. This extra Ni atom in FH composition is on the top of the FH valence band. This induces a change in the top of the valence band maxima (VBM) and conduction band minima (CBM) of FH phase. Therefore, it is pushed up to higher energy as compared to that of the corresponding HH composition. Through this MOT, one can anticipate the formation of a heterojunctions (staggered gap) at HH/FH interface in HH$(1-x)$/FH$(x)$ composites. The energy barrier or offset between CBM of HH and FH acts as an energy filter for conduction electrons within the conduction band (CB) of HH. The height of this energy barrier depends on the CBM position of the FH phase. The CBM of FH inclusions usually depends on the size of the FH inclusions under quantum confinement regime. Therefore, the relative

reductions in carrier density measured in HH$(1-x)$/FH$(x)$ composites in $ZrNi_{1+x}Pb_{0.38}Sn_{0.6}Bi_{0.02}$ with $x = 0.01$ and 0.03 around room temperature correspond to the fraction of low-energy conduction electrons from the CB of the HH matrix trapped by the energy barrier at the HH/FH interfaces. The fraction of low-energy electrons trapped by the energy barrier increases with the increasing density of HH/FH interfaces within the composites, but at the same time decreases with the increasing size of FH inclusions (decreasing energy barrier). The deliberate excess of Ni concentration in HH is reducing the band of composite as compared to pure HH. This is presented clearly on the basis of MOT diagram to show the heterojunction formation at interface of ZrNiPb (HH)/ZrNi2Pb (FH) composite. This MOT diagram relates to the present composition of $ZrNi_{1+x}Pb_{0.38}Sn_{0.6}Bi_{0.02}$ $(0 \leq x \leq 0.07)$ composite samples in which $ZrNiPb_{0.38}Sn_{0.6}Bi_{0.02}$ represents the HH alloy and $ZrNi_2Pb_{0.38}Sn_{0.6}Bi_{0.02}$ corresponds to FH alloy.

Figure 5 displays the relation between the temperature and power factor (PF) for all the synthesized compositions $ZrNi_{1+x}Pb_{0.38}Sn_{0.6}Bi_{0.02}$ $(0 \leq x \leq 0.07)$ composites alloys. The sample $ZrNi_{1.03}Pb_{0.38}Sn_{0.6}Bi_{0.02}$ reflects maximally enhanced PF as compared to $ZrNiPb_{0.38}Sn_{0.6}Bi_{0.02}$ HH matrix. A maximum PF of $75 \times 10^{-2}$ W mK$^{-2}$ at 773 K is achieved for $ZrNi_{1.03}Pb_{0.38}Sn_{0.6}Bi_{0.02}$, which is $\sim 42\%$ higher than that of $ZrNiPb_{0.38}Sn_{0.6}Bi_{0.02}$ HH. This high value of PF is evidently attributed to a simultaneous increase in $\alpha$ and $\sigma$.

### 3.3 *Thermal transport properties*

Further, we discuss our results of thermal conductivity ($\kappa$) in $ZrNi_{1+x}Pb_{0.38}Sn_{0.6}Bi_{0.02}$ $(0 \leq x \leq 0.07)$ composite samples. Figure 6a–c elucidates the calculated
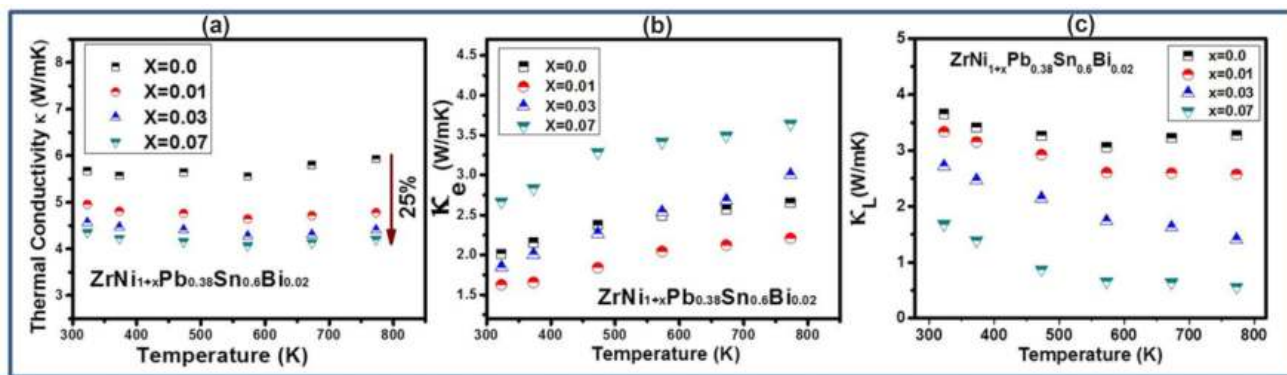
**Figure 6.** (**a**) Total thermal conductivity, (**b**) electronic, (**c**) lattice thermal conductivity of $ZrNi_{1+x}Pb_{0.38}Sn_{0.6}Bi_{0.02}$ ($0 \leq x \leq 0.07$) with temperature variations.

temperature-dependent total thermal conductivity ($\kappa$) with corresponding lattice thermal conductivity ($\kappa_L$) and electronic thermal conductivity ($\kappa_e$) contributions for all the alloys. Herein, a significant reduction in $\kappa$ was observed in $ZrNi_{1+x}Pb_{0.38}Sn_{0.6}Bi_{0.02}$ ($0 \leq x \leq 0.07$) composite samples as compared to $ZrNiPb_{0.38}Sn_{0.6}Bi_{0.02}$ HH with a simultaneous increase in PF. The variation of $\kappa$ with temperature is displayed in figure 6a for all the samples. In all the samples, $\kappa$-value was reduced with an increase in temperature, which implies the dominancy of lattice conductivity. The reduction in $\kappa$-values was observed with increasing Ni content in the samples. The sample having $ZrNi_{1.07}Pb_{0.38}Sn_{0.6}Bi_{0.02}$ composition depicts the lowest $\kappa$-value $\sim 4.2$ W mK$^{-1}$ at 773 K, which is $\sim 25\%$ inferior to $ZrNiPb_{0.38}Sn_{0.6}Bi_{0.02}$ HH. The decreasing value of $\kappa$ could be attributed to the facile scattering of phonons at various grains and phase boundaries along with their interfaces that was optimally achieved through compositional tuning approach. The Wiedemann–Franz law was applied to obtain $\kappa_e$ via relation $\kappa_e = L\sigma T$, where $L$ is the Lorentz number, electrical conductivity ($\sigma$), and temperature ($T$). And $\kappa_L$ value was calculated by subtracting $\kappa_e$ value from $\kappa$-value [29]. The exact value of $\kappa_e$ is achieved by calculating correct estimation of $L$ with temperature. The temperature-dependent $L$ for all the samples is displayed in figure 7a. Figure 7b presents $L$ *vs.* $\alpha$ for the entire composite samples and also with the estimated $L$-value through the SPB-APS model [30] or can be described as a single parabolic band with an acoustic phonon scattering model. This fitting also shows the degenerated limit of the Lorentz number $L = 2.4 \times 10^{-8}$ W ohm K$^{-2}$ [30].

Figure 6b displays the temperature variation of $\kappa_e$ for $ZrNi_{1+x}Pb_{0.38}Sn_{0.6}Bi_{0.02}$ ($0 \leq x \leq 0.07$) composite samples. An increased value of $\kappa_e$ is observed with increasing temperature in all composites, which is consistent with $\sigma$ data. We observe that $\kappa_L$, figure 6c, decreases with rising temperature, displaying a similar trend as we acquired in $\kappa$. Thus, the reduction in $\kappa$ is mainly attributable to the drastic reduction in $\kappa_L$. The observed reduction in $\kappa_L$ for $ZrNi_{1+x}Pb_{0.38}Sn_{0.6}Bi_{0.02}$ ($0 \leq x \leq 0.07$) composites samples are due to coherent

nano-range boundaries of HH and FH, which efficiently scatter mid-frequency phonons in addition to longer one at grain boundaries within these composites [11–13].

### 3.4 *Thermoelectric figure-of-merit (ZT)*

Figure 8a shows ZT variation with temperature in $ZrNi_{1+x}Pb_{0.38}Sn_{0.6}Bi_{0.02}$ ($0 \leq x \leq 0.07$) composites. Irrespective of the temperature, the ZT value for $ZrNi_{1+x}Pb_{0.38}Sn_{0.6}Bi_{0.02}$ composites increases with rising temperature.

A substantial increase in ZT $\approx 1.3$ at a temperature of 773 K is achieved for $ZrNi_{1.03}Pb_{0.38}Sn_{0.6}Bi_{0.02}$ which is considerably higher value as compared to $ZrNiPb_{0.38}Sn_{0.6}Bi_{0.02}$ HH matrix phase (ZT $\approx 0.67$ at 773 K). Thus, a synergistic increase in $\alpha \sim 12\%$ and $\sigma \sim 15\%$, and a reduction of $\sim 25\%$ in $\kappa$, results in about 90% enhancement in the ZT value for $ZrNi_{1.03}Pb_{0.38}Sn_{0.6}Bi_{0.02}$ in comparison to that of pristine HH. Whereas, $ZrNi_{1.07}Pb_{0.38}Sn_{0.6}Bi_{0.02}$ composite, which is semi-metallic in nature, exhibited the largest reduction in $\kappa$ but could not attain a large ZT value due to very low $\alpha$. Hence, a high concentration of FH in the composite is not profitable for enhancing ZT value. The present system of HH composite has reasonably high value of ZT as compared to other state-of-the-art *n*-type HH TE materials [30], including NiCoSb (ZT $\sim 0.4$ @ 973 K), ZrNiPb (ZT $\sim 0.6$ @ 873 K), $Nb_{0.8}Ti_{0.2}FeSb$ (ZT $\sim 1.0$ @ 973 K), $Hf_{0.44}Zr_{0.44}Ti_{0.12}Sb_{0.8}Sn_{0.2}$ (ZT $\sim 0.4$ @ 973 K), and $Hf_{0.8}Ti_{0.2}CoSb_{0.8}Sn_{0.2}$ (ZT $\sim 0.9$ @ 1073 K). Moreover, these composites are free from hafnium (Hf), which makes these materials cost-effective for TE device fabrication [6].

### 3.5 *Compatibility factor*

TE compatibility factor (*S*) was estimated for all $ZrNi_{1+x}Pb_{0.38}Sn_{0.6}Bi_{0.02}$ samples. This factor is used for compatible
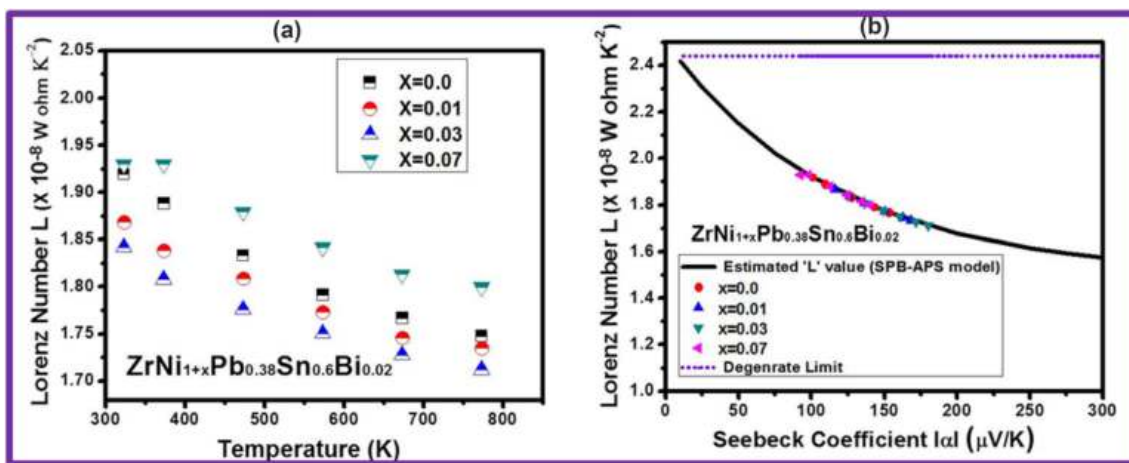
**Figure 7.** (a) *L*-value variation with temperature for ZrNi$_{1+x}$Pb$_{0.38}$Sn$_{0.6}$Bi$_{0.02}$ ($0 \leq x \leq 0.07$) composites samples. (b) $\alpha(T)$-dependent *L*-value for ZrNi$_{1+x}$Pb$_{0.38}$Sn$_{0.6}$Bi$_{0.02}$ ($0 \leq x \leq 0.07$) composite samples.
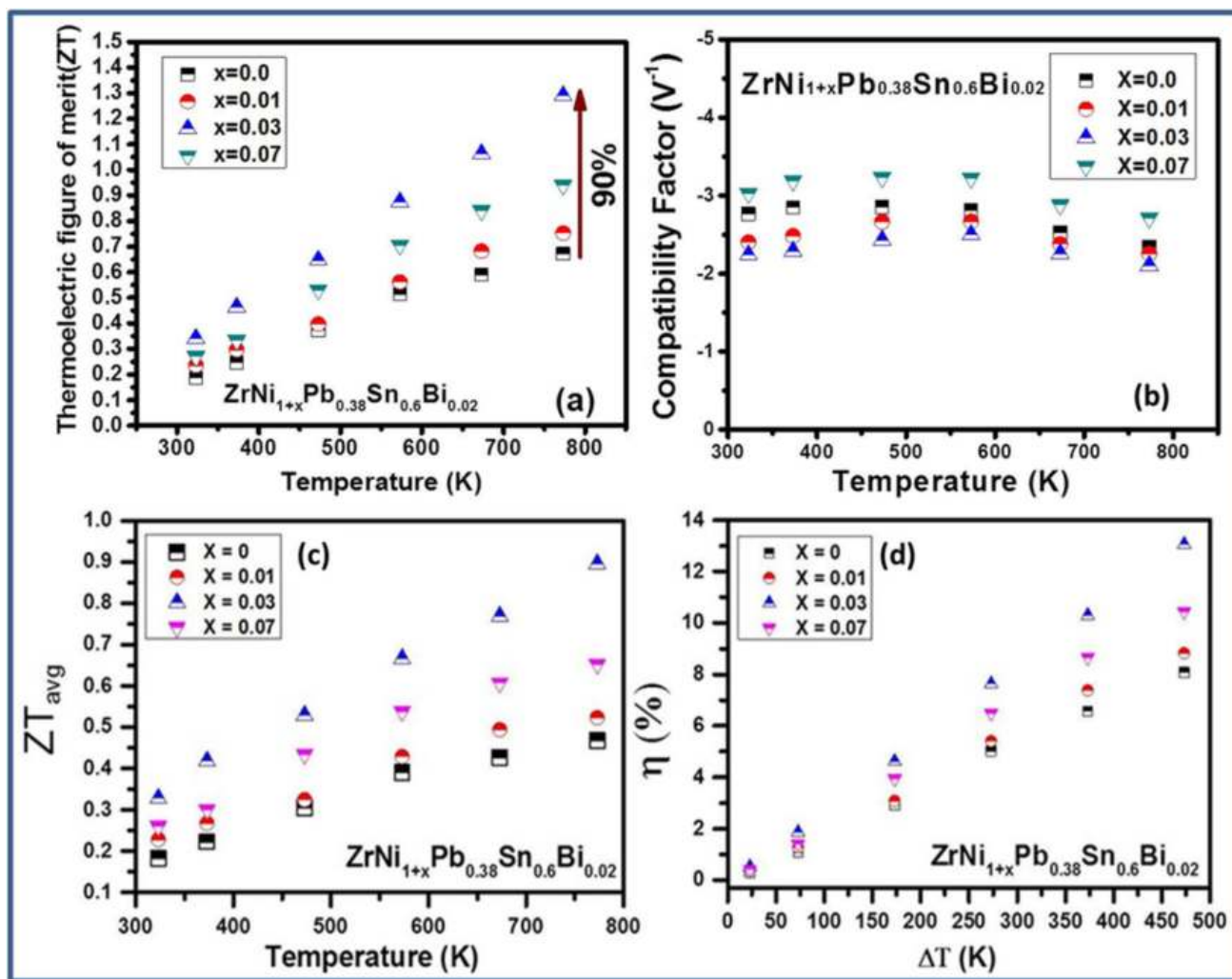


**Figure 8.** (a) Thermoelectric figure-of-merit (ZT) variation with temperature in ZrNi$_{1+x}$Pb$_{0.38}$Sn$_{0.6}$Bi$_{0.02}$ ($0 \leq x \leq 0.07$) composites samples. (b) Display of the temperature-dependent TE compatibility factor for ZrNi$_{1+x}$Pb$_{0.38}$Sn$_{0.6}$Bi$_{0.02}$ ($0 \leq x \leq 0.07$) composites samples. (c) Temperature-dependent ZT average (ZT$_{avg}$) values for ZrNi$_{1+x}$Pb$_{0.38}$Sn$_{0.6}$Bi$_{0.02}$ ($0 \leq x \leq 0.07$) composites samples. (d) Theoretically calculated thermoelectric device efficiency with $\Delta T$ for ZrNi$_{1+x}$Pb$_{0.38}$Sn$_{0.6}$Bi$_{0.02}$ ($0 \leq x \leq 0.07$) composites samples.

segmentation in TE devices for waste heat recovery applications. This is defined as follows [31],

$$S = \frac{\sqrt{1 + ZT}}{\alpha T} - \frac{1}{\alpha T}, \qquad (3)$$

where temperature ($T$) and Seebeck coefficient ($\alpha$). The value of $S$ is required for finding the best-suited counterpart and to achieve maximum TE efficiency in a TE device. The $S$-value of $ZrNi_{1.03}Pb_{0.38}Sn_{0.6}Bi_{0.02}$ ($\sim -2.7$ $V^{-1}$ at 773 K) composite is boosted up by $\sim 17\%$ as to the parent $ZrNiPb_{0.38}Sn_{0.6}Bi_{0.02}$ ($-2.3$ $V^{-1}$ at 773 K) HH, as shown in figure 8b. Moreover, the value of $S$ for $ZrNi_{1.03}Pb_{0.38}Sn_{0.6}Bi_{0.02}$ sample calculated and found to be here is comparable to other $n$-type TE materials [32], which includes $Ti_{0.5}(ZrHf)_{0.5}NiSn$ ($S \sim -2.8$ $V^{-1}$ @ 973 K), $Si_{0.78}Ge_{0.22}$ ($S \sim -1.7$ $V^{-1}$ @ 1000 K), $Bi_2Te_3$ ($S \sim -2.5$ $V^{-1}$ @ 573 K) MnSiSn ($S \sim -1.7$ $V^{-1}$ @ 873 K) and $La_3Te_4$ ($S \sim -1.3$ $V^{-1}$ at 1273 K). We find that $ZrNi_{1.03}Pb_{0.38}Sn_{0.6}Bi_{0.02}$ is well well-suited $n$-type TE compound for segmentation with other TE materials, as displayed in figure 8b. Therefore, the twofold benefits of a large value of ZT and decent $S$-value create these $ZrNi_{1+x}Pb_{0.38}Sn_{0.6}Bi_{0.02}$ ($0 \leq x \leq 0.07$) materials to be an excellent material for efficient TE device fabrication [32].

For more clear evidence towards achieving high ZT in $ZrNi_{1+x}Pb_{0.38}Sn_{0.6}Bi_{0.02}$ composite compounds, we have estimated the theoretical conversion efficiency of TE device by using the following equation:

$$\eta = \frac{\Delta T}{T_h} \frac{\sqrt{1 + ZT_{avg}} - 1}{\sqrt{1 + ZT_{avg}} + \frac{T_c}{T_h}}, \qquad (4)$$

where $\Delta T$ is the difference in temperature of hot temperature ($T_h$) and cold temperature ($T_c = 300$ K) and $ZT_{avg}$ represents the average ZT value as calculated by the given equation [33]:

$$ZT_{avg} = \frac{\int_{T_c}^{T_h} ZT dt}{T_h - T_c}, \qquad (5)$$

here, the device theoretical conversion efficiency value for optimized composite sample $ZrNi_{1.03}Pb_{0.38}Sn_{0.6}Bi_{0.02}$ is estimated at $\sim 13.6\%$, which is an acceptable value for commercial TE device fabrication. Figure 8c shows a relation between temperature and average ZT value ($ZT_{avg}$) for all the compositions $ZrNi_{1+x}Pb_{0.38}Sn_{0.6}Bi_{0.02}$ ($0 \leq x \leq 0.7$) composites samples. The theoretically calculated TE device conversion efficiency (with increasing $\Delta T$) for $ZrNi_{1+x}Pb_{0.38}Sn_{0.6}Bi_{0.02}$ composite samples is displayed in figure 8d. We strongly believe that these compositionally tuned $n$-types HH-based composite TE materials provide an effective pathway for the industrialization of TE devices, which are highly efficient and cost-effective [30].

## 4. Conclusion

In conclusion, compositional tuning approach has been employed to synthesize a series of alloys having the composition $ZrNi_{1+x}Pb_{0.38}Sn_{0.6}Bi_{0.02}$ ($0 \leq x \leq 0.07$). A substantially enhanced value of ZT $\sim 1.3$ (at 773 K) is achieved for $ZrNi_{1.03}Pb_{0.38}Sn_{0.6}Bi_{0.02}$, which is $\sim 90\%$ higher as compared to the pristine $ZrNi_{1.03}Pb_{0.38}Sn_{0.6}Bi_{0.02}$ HH alloy. This improved ZT is ascribed to higher PF ($75 \times 10^{-2}$ W mK$^{-2}$ at 773 K) and reduced thermal conductivity, which is nearly $\sim 25\%$ lower than pristine HH alloy. It is noted that increasing Ni concentration provides multiple sizes of FH inclusion in the HH matrix for facile phonon scattering, which significantly reduces lattice thermal conductivity. Moreover, a low-energy electron filtering at the interface results in a higher value of the Seebeck coefficient leading to enhanced PF. The TE compatibility factor ($S$) for $x = 0.03$ is estimated $\sim -2.7$ $V^{-1}$ at 773 K, which is $\sim 17\%$ higher than the pristine composition. The composition $ZrNi_{1.03}Pb_{0.38}Sn_{0.6}Bi_{0.02}$ has revealed twofold benefits of enhanced ZT along with appreciable $S$-value that provides excellent pathway for efficient TE device fabrication. The theoretically calculated TE device efficiency is estimated for all the compositions and a value of $\eta \sim 13.6\%$ is achieved for $ZrNi_{1.03}Pb_{0.38}Sn_{0.6}Bi_{0.02}$. Our results imply that the compositional tuning approach holds great potential for achieving new TE alloys with high conversion efficiency.

## References

[1] Nolas G S, Sharp J and Goldsmid J 2001 *Springer Science and Business Media* **45** 293
[2] Ma Z, Wei J, Song P, Zhang M, Yang L, Ma J *et al* 2021 *Mater. Sci. Semicond. Process.* **121** 105303
[3] Kumar A, Bano S, Govind B, Bhardwaj A, Bhatt K, Misra D K *et al* 2021 *J. Electronic Mater.* **50** 6037
[4] Li W, Nozariasbmarz A, Kishore R A, Kang H B, Dettor C, Zhu H *et al* 2021 *ACS Appl. Mater. Interface* **13** 53935
[5] Jiang S and Yang K 2021 *J. Alloys Compd.* **867** 158854
[6] Zhu T, Fu C, Xie H, Liu Y and Zhao X 2015 *Adv. Energy Mater.* **5** 1500588
[7] Amatya R and Ram R J 2010 *J. Electron. Mater.* **41** 1019
[8] Schmitt J, Gibbs Z M, Snyder G J and Felser C 2015 *Mater. Horiz.* **2** 75
[9] Gałązka K, Xie W, Populoh S, Aguirre M H, Yoon S, Büttner G *et al* 2020 *Rare Metals* **39** 659
[10] Ren Q, Fu C, Qiu Q, Dai S, Liu Z, Masuda T *et al* 2020 *Nat. Commun.* **11** 3142

[11] Sahoo P, Liu Y, Makongo J P A, Su X L, Kim S J, Takas N *et al* 2013 *Nanoscale* **5** 9427

[12] Makongo J P A, Misra D K, Zhou X, Pant A, Shabetai M R, Su X *et al* 2011 *J. Am. Chem. Soc.* **133** 18852

[13] Chauhan N S, Bhardwaj A, Senguttuvan T S, Pant R P, Mallik R C, Misra D K *et al* 2016 *J. Mater. Chem. C* **4** 5778

[14] Chen K, Zhang R, Bos J W G and Reece M J 2022 *J. Alloys Compd.* **892** 162045

[15] Bhardwaj A, Chauhan N S, Sancheti B, Pandey G N, Senguttuvan T D, Misra D K *et al* 2015 *Phys. Chem. Chem. Phys.* **17** 30090

[16] Li X, Yang P, Wang Y, Zhang Z, Qin D, Xue W *et al* 2020 *AAAS Res.* **9** 2020

[17] Biswas K, He J, Blum I D, Wu C I, Hogan T P, Seidman D N *et al* 2012 *Nature* **489** 418

[18] Mao J, Zhou J, Zhu H, Liu Z, Zhang H, He R *et al* 2017 *Chem. Mater.* **29** 867

[19] Guo S D 2016 *RSC Adv.* **6** 47958

[20] Yousuf S and Gupta D C 2019 *Res. Phys.* **12** 1386

[21] Pei Y, Wang H and Snyder G J 2012 *Adv. Mater.* **24** 6125

[22] Romaka V V, Rogl P, Romaka L, Stadnyk Y, Melnychenko N, Grytsiv A *et al* 2013 *J. Solid State Chem.* **197** 112

[23] Chai Y W, Oniki T and Kimura Y 2015 *Acta Mater.* **85** 300

[24] Makongo J, Zhou X, Misra D K, Uher C and Poudeu P F P 2013 *J. Solid State Chem.* **201** 287

[25] Faleev S V and Leonard F 2008 *Phys. Rev. B* **77** 214304

[26] Nolas G S, Sharp J and Goldsmid H J 2021 Springer, Berlin, 2021

[27] Bytenskii L I, Gudkin T S, Iordanishvili E K, Kazmin S A, Kaidanov V I, Nemov S A *et al* 1977 *Semiconductors* **11** 894

[28] Liu W S, Zhang B P, Li J F, Zhang H L and Zhao L D 2007 *J. Appl. Phys.* **102** 103717

[29] Kim H S, Gibbs Z M, Tang Y, Wang H and Snyder G J 2015 *APL Mater.* **3** 041506

[30] Mao J, Liu Z, Zhou J, Zhu H, Zhang Q, Chen G *et al* 2018 *Adv. Phys.* **67** 69

[31] Snyder G J and Ursell T S 2003 *Phys. Rev. Lett.* **91** 148301

[32] Ngan P H, Christensen D V, Snyder G J, Hung L T, Linderoth S, Nong N V *et al* 2014 *Phys. Status Solidi. A* **211** 9

[33] Kim H S, Liu W and Rem Z 2017 *Energy Environ. Sci.* **10** 69